JGR Space Physics

RESEARCH ARTICLE
10.1029/2020JA028027

Cross-Scale Quantification of Storm-Time Dayside Magnetospheric Magnetic Flux Content

M. Akhavan-Tafti[1,2], D. Fontaine[1], J. A. Slavin[2], O. Le Contel[1], and D. Turner[3]

[1]Laboratoire de Physique des Plasmas (LPP), École Polytechnique, CNRS, Sorbonne Université, Institut Polytechnique de Paris, Palaiseau, France, [2]Climate and Space Sciences and Engineering (CLaSP), University of Michigan, Ann Arbor, MI, USA, [3]Applied Physics Laboratory (APL), Johns Hopkins University, Laurel, MD, USA

Abstract A clear understanding of storm-time magnetospheric dynamics is essential for a reliable storm forecasting capability. The dayside magnetospheric response to an interplanetary coronal mass ejection (ICME; dynamic pressure $P_{dyn} > 20$ nPa and storm-time index SYM-H < -150 nT) is investigated using in situ OMNI, Geotail, Cluster, MMS, GOES, Van Allen Probes, and THEMIS measurements. The dayside magnetic flux content is directly quantified from in situ magnetic field measurements at different radial distances. The arrival of the ICME, consisting of shock and sheath regions preceding a magnetic cloud, initiated a storm sudden commencement (SSC) phase (SYM-H ~ +50 nT). At SSC, the magnetopause standoff distance was compressed earthward at ICME shock encounter at an average rate ~−10.8 Earth radii per hour for ~10 min, resulting in a rapid 40% reduction in the magnetospheric volume. The "closed" magnetic flux content remained constant at 170 ± 30 kWb inside the compressed dayside magnetosphere, even in the presence of dayside reconnection, as evident by an outsized flux transfer event containing 160 MWb. During the storm main and recovery phases, the magnetosphere expanded. The dayside magnetic flux did not remain constant within the expanding magnetosphere (110 ± 30 kWb), resulting in a 35% reduction in pre-storm flux content during the magnetic cloud encounter. At that stage, the magnetospheric magnetic flux was eroded resulting in a weakened dayside magnetospheric field strength at radial distances $R \geq 5$ R_E. It is concluded that the inadequate replenishment of the eroded dayside magnetospheric flux during the magnetosphere expansion phase is due to a time lag in storm-time Dungey cycle.

Plain Language Summary A clear understanding of Earth's magnetospheric dynamics is essential for a reliable space weather forecasting capability. To achieve this, we take advantage of the Heliophysics System Observatory's (HSO) multitude of in situ observations in order to, for the first time, quantify the amount of magnetic flux stored in the dayside magnetosphere. The stored magnetic flux shields our ground-based and space-borne assets from adverse space weather events. We examine the dayside magnetic flux content during an encounter with an interplanetary coronal mass ejection (ICME). ICME is a large-scale bundle of magnetic flux and charged particles originating from the Sun. Upon arrival, the ICME which occupied nearly one third of the space between the Sun and Earth forced the dayside magnetosphere to rapidly shrink down to geosynchronous orbit where most communications and weather satellites are located. Though the dayside magnetosphere significantly shrunk, its magnetic flux content remained constant. It was only when the dayside magnetosphere started to expand that the dayside magnetospheric flux content gradually reduced by 35%. It is concluded that, during large ICME encounters, the rate at which dayside magnetic flux is transported to the magnetotail is faster than the rate at which magnetic flux is recycled, via a process known as the Dungey cycle. In addition to the observed loss in magnetic flux, this time lag in Dungey cycle can further cause magnetopause shadowing, wherein significant population of magnetospheric charged particles is lost to solar wind.

Key Points:
- Dayside closed magnetic flux is quantified during an interplanetary coronal mass ejection encounter using cross-scale observations
- Closed magnetic flux remains constant inside the reconnecting dayside magnetosphere compressed by 70% in storm sudden commencement phase
- Dayside closed magnetic flux is reduced by 35% in storm main phase, indicating a time lag in storm-time Dungey cycle

Supporting Information:
- Supporting Information S1
- Figure S1

Correspondence to:
M. Akhavan-Tafti,
akhavant@umich.edu

Citation:
Akhavan-Tafti, M., Fontaine, D., Slavin, J. A., Le Contel, O., & Turner, D. (2020). Cross-scale quantification of storm-time dayside magnetospheric magnetic flux content. *Journal of Geophysical Research: Space Physics*, *125*, e2020JA028027. https://doi.org/10.1029/2020JA028027

Received 19 MAR 2020
Accepted 1 OCT 2020
Accepted article online 14 OCT 2020

1. Introduction

Interplanetary coronal mass ejections (ICMEs) carry mass and magnetic field expelled from closed field regions of the Sun that were previously not participating in the solar wind expansion (e.g., Gosling, 1990). Generally, ICMEs consist of three principal large-scale structures, including a leading shock wave followed by a dense sheath and a well-formed, force-free (e.g., Burlaga, 1988) magnetic flux rope, also referred to as a magnetic cloud. The magnetic flux rope is often characterized by a smooth magnetic field rotation, low

plasma beta (β) defined as the ratio of thermal to magnetic pressures, and low Alfvénic Mach number, $M_A \propto \sqrt{n}/B$, where n and B denote local plasma density and magnetic field strength.

The general relationship between variations in the solar wind physical parameters and magnetospheric activity is well known (e.g., Akasofu, 1981). However, the geomagnetic activity is more complex under extreme space weather events. In particular, there is increasing interest in determining the geomagnetic responses to the drivers of geomagnetic storms, defined as intervals of intense and long-lasting interplanetary convection electric field ($E = -v_i \times B$, where v_i is the ion bulk flow velocity) that lead to a sufficiently intensified ring current (Gonzalez et al., 1994). The variations in the ring current intensity are parameterized by storm-time indices, such as Dst (1-hr resolution) and SYM-H (1-min resolution) indices (e.g., Wanliss & Showalter, 2006).

The flows and magnetic fields of ICMEs can greatly distort the interplanetary magnetic field (IMF) (Baker, 2000). Gonzalez et al. (2002) indicated that intense geomagnetic storms, defined as $-250 \leq$ Dst [nT] < -100, were often associated with the ICME sheath and magnetic cloud. Similarly, Meng et al. (2019) showed that most superstorms, defined as Dst [nT] ≤ -250, were driven by the ICME sheath or a combination of sheath and a magnetic cloud. The ICME sheath was further shown to become more geoeffective with increasing ICME speed (Kilpua et al., 2017), and the magnetic cloud geoeffectiveness was enhanced during times of smooth and strong southward IMF orientation (Gonzalez et al., 2002).

While the majority of solar wind plasma is effectively shielded from entering into the magnetosphere, a fraction of the solar wind plasma can diffuse into the magnetosphere. At the dayside magnetopause, the shocked "open" IMF comes in contact with the "closed" (both ends connected to the magnetized body) magnetospheric field. Depending on the magnetic field orientations and environmental conditions, IMF and magnetospheric field lines may break and rearrange through a process known as magnetic reconnection (i.e., Burch & Phan, 2016). The resulting reconnected field lines are connected to the IMF on one end ("open") and to the magnetized body on the other end, providing a pathway for the solar wind plasma to enter the magnetosphere (and for magnetospheric plasma to escape). These newly opened field lines are then convected to the nightside by the solar wind where they contribute to the magnetotail magnetic flux and plasma content. When in the magnetotail, these field lines reconnect again which results in the creation of closed field lines which then return to the dayside magnetopause to replenish the previously eroded magnetic flux. This repeatable process is known as the Dungey cycle (Dungey, 1961). A time lag between the dayside and nightside reconnections can result in an open-flux pileup (e.g., Milan et al., 2003, 2006; Russell, 1972).

A clear understanding of the storm-time magnetospheric dynamics is essential for improving the space weather forecasting and mitigation procedures. In this study, we report cross-scale observations of storm-time magnetospheric dynamics during an ICME event encounter. In particular, the storm-time magnetopause standoff distance and the magnetospheric total "closed" magnetic flux are directly quantified. The magnetospheric response to the ICME event is then compared with that of two independent ICMEs.

1.1. Overview of a Chain of Three ICMEs

The magnetic field and plasma measurements in the solar wind for a chain of three ICMEs spanning 12 December 2015 to 12 January 2016 are obtained from the OMNI (King & Papitashvili, 2005) data set. Figure 1 provides storm-time physical parameters, including (a) storm-time index SYM-H, (b) IMF magnetic field magnitude and vector, (c) ion velocity vector, (d) dynamic pressure, and (e) plasma beta and Alfvénic Mach number ($M_A = V_{SW}/V_A$, where V_{SW} and V_A represent solar wind flow and Alfvén speeds). All vectors are in the Geocentric Solar Ecliptic (GSE) coordinate system.

The first ICME, labeled as "ICME 1", arrived at Earth on 13 December 2015. Before the ICME arrival, the interplanetary environment was relatively quiet as indicated by SYM-H ~ 0 [nT] and $M_A \sim 10$. The IMF magnitude jumped sharply across the ICME shock, at which point SYM-H increased, indicating a storm sudden commencement (SSC) phase. The ICME shock was followed by a sharp southward rotation of IMF B_z ($B_z < -10$ nT) and an increase in dynamic pressure ($P_{\mathrm{dyn}} > 30$ nPa). At this point, SYM-H was reduced to -50 nT. Plasma beta and M_A were also significantly reduced inside the ICME, before fully recovering by 18 December 2015.

On 19 December 2015, shortly after the interplanetary environment had returned to average conditions, a second ICME reaches the Earth's magnetosphere. "ICME 2" composed of a shock and sheath region

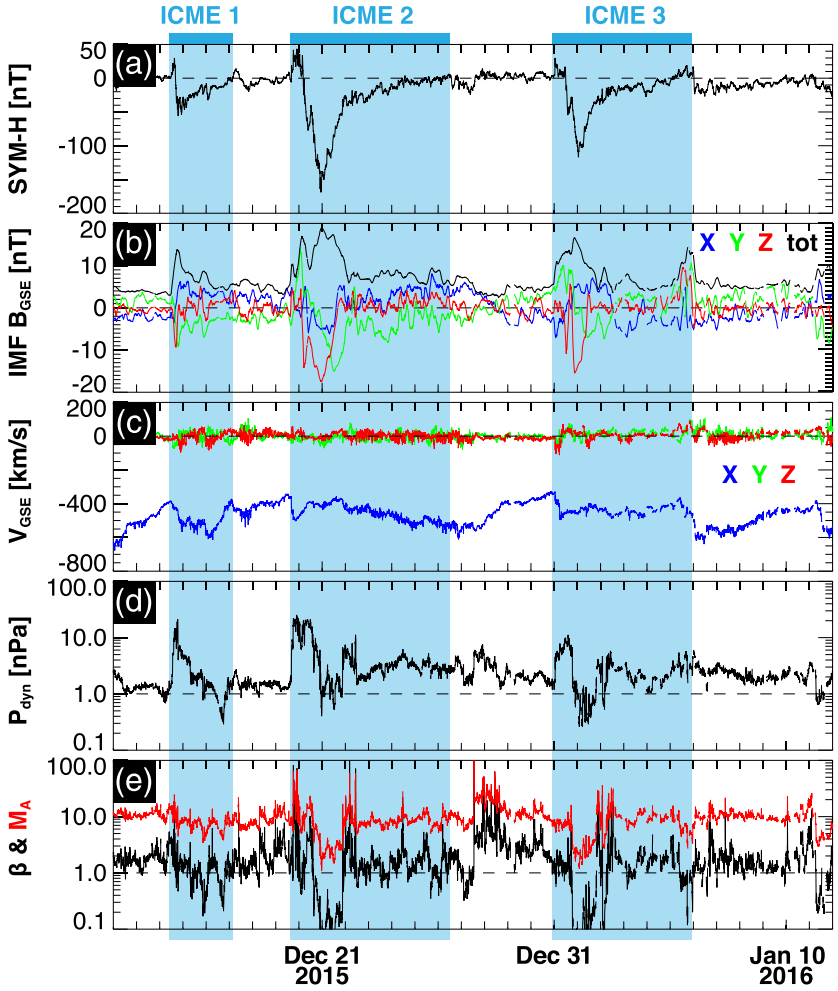

Figure 1. Solar wind conditions during 12 December 2015 to 12 January 2016. The panels include (a) storm-time index SYM-H, (b) IMF magnetic field (3-hr resolution) magnitude and vector, (c) ion velocity vector, (d) dynamic pressure, and (e) plasma beta (black) and Alfvénic Mach number (red; $M_A = V_{SW}/V_A$, where V_{SW} and V_A represent solar wind flow and Alfvén speeds). All vectors are in Geocentric Solar Ecliptic (GSE) coordinate systems. Storm events, including the SSC, main, and recovery phases corresponding to ICMEs 1–3, are shaded with light blue columns.

preceding a magnetic cloud. At the shock, IMF $|B|$ and dynamic pressure jumped by a factor of 4, and SYM-H reached almost +50 nT. Within the ICME sheath region, SYM-H reduced to a first minimum, SYM-H ~ −75 nT. The storm finally reached a peak strength of SYM-H < −150 nT at the core region of the magnetic cloud where IMF B_z ~ −20 nT and P_{dyn} ~ 20 nPa.

Inside the magnetic cloud ($|B|$ = 20 nT and $n_i = 40\ \mathrm{cm}^{-3}$), both plasma beta and M_A were reduced sharply. Plasma beta and M_A dropped by more than an order of magnitude in the leading part of the magnetic cloud while B_z remained dominant and southward. From a planetary perspective, once inside the magnetic cloud, the interplanetary environment impacting the Earth's magnetosphere became more typical of that near the orbital distance of Mercury (Sarantos & Slavin, 2009; Winslow et al., 2013). Closer to the Sun, plasma beta and Alfvénic Mach number are smaller than Earth's, under average solar wind conditions (β = 0.5–0.9 and M_A = 3.9–5.7 at Mercury; Slavin & Holzer, 1981). After the passage of ICME 2, the interplanetary environment returned to average conditions.

The SSC of 31 December 2015 corresponds to the arrival of a third ICME. Inside the "ICME 3" sheath region, SYM-H reached −50 nT and plasma density and P_{dyn} increased. Inside the magnetic cloud, $|B|$ increased while β and M_A sharply decreased. Also, at the leading edge of the magnetic cloud SYM-H < −100 nT.

Table 1
The Physical Properties of the Three ICMEs

	SYM-H [nT]	Max ($\lvert B_{MC}\rvert$)[a, b] [nT]	V_{SW} [km/s]	MC diameter[c] [R_E]	Max (P_{dyn})[d] [nPa]	SH-MC[e] β	SH-MC M_A
ICME 1	−50	15	450	1,500	20	3–1	10–8
ICME 2	−150	20	400	8,000	20	10–0.05	20–2
ICME 3	−100	15	425	4,500	10	1–0.05	6–2

[a]Magnetic cloud is referred to as "MC." [b]Maximum magnetic field magnitude inside the magnetic cloud. [c]Magnetic cloud diameter is estimated as diameter = V_{SW} × duration. [d]Maximum solar wind dynamic pressure. [e]The ICME sheath is referred to as "SH."

Table 1 summarizes the physical properties of the three ICMEs. The physical parameters of interest include storm-time index SYM-H, magnetic cloud peak magnetic field magnitude, average ion speed, estimated magnetic cloud diameter assuming cylindrical symmetry (Akhavan-Tafti et al., 2018), maximum dynamic pressure, and IMF beta and Alfvénic Mach number in the ICME sheath (SH) and magnetic cloud (MC).

Among the three ICMEs, ICME 2 was associated with the strongest geomagnetic activity (SYM-H < −150 nT). The magnetic cloud of ICME 2 was the largest in dimensions and had the greatest $|B|$ at its core region. The ratios of the sheath to magnetic cloud plasma beta (200) and Alfvénic Mach number (10) were most significant for ICME 2. Similarly, compared to ICME 1, the ratios of sheath to magnetic cloud β (20) and M_A (3) were greater in ICME 3. Unlike ICME 1 with smooth main phase and recovery phase SYM-H profiles, ICMEs 2 and 3 showed double-dip SYM-H signatures during the main phases (first dip from sheath and second dip from the magnetic cloud).

In the remaining sections, the magnetospheric response to ICME 2 is discussed. Finally, in section 3, the magnetospheric responses to ICMEs 1 and 3 are presented and compared with ICME 2.

1.2. Storm-Time Magnetopause Standoff Distance

The enhanced dynamic pressures and southward IMF B_z during ICME arrival can change the magnetopause standoff distance. In particular, Shue et al. (1997) provided an empirical functional form to fit the size and shape of the magnetopause:

$$r = r_0\left(P_{\mathrm{dyn}}, B_z\right)\left(\frac{2}{1+\cos(\phi)}\right)^{\alpha\left(P_{\mathrm{dyn}}, B_z\right)}$$

where ϕ is the angle between the Earth-Sun line and the direction of r. This functional form, which was later improved for extreme space weather events (Shue et al., 1998), relies on two parameters, r_0 and α, representing the standoff distance and the level of tail flaring:

$$r_0 = \begin{cases} \left(11.4 + 0.013\, B_z\right)\left(P_{\mathrm{dyn}}\right)^{-\frac{1}{6.6}}, & B_z \geq 0 \\ \left(11.4 + 0.14\, B_z\right)\left(P_{\mathrm{dyn}}\right)^{-\frac{1}{6.6}}, & B_z < 0 \end{cases}$$

where $\alpha = (0.58 - 0.010\, B_z)(1 + 0.010\, P_{\mathrm{dyn}})$.

Figure 2a shows a time series plot of SYM-H profile during ICME 2. The interval is divided into six subintervals, as marked by the various shadings. Figure 2b shows the modeled magnetopause standoff distance in the XY plane for the duration of ICME 2, that is, 18–29 December 2015. The shaded curves indicate the magnetopause boundary which are derived using the Shue model where the input dynamic pressure and IMF B_z magnitude and polarity are the OMNI observations. The shading of the curves corresponds to the subintervals in panel (a).

The modeled magnetopause standoff distance values are further validated by in situ MMS (Burch et al., 2016) and Cluster (Escoubet et al., 1997) observations. The empirical Shue magnetopause model indicates that the solar wind dynamic pressure enhancements and IMF B_z variations can change the magnetopause standoff distance, causing compression of the magnetosphere. Here, the Shue model is used to estimate the magnetopause standoff distance and to estimate the magnetospheric volume based on the in situ OMNI solar wind measurements. The Shue model is an azimuthally symmetrical elliptical surface with location defined by a

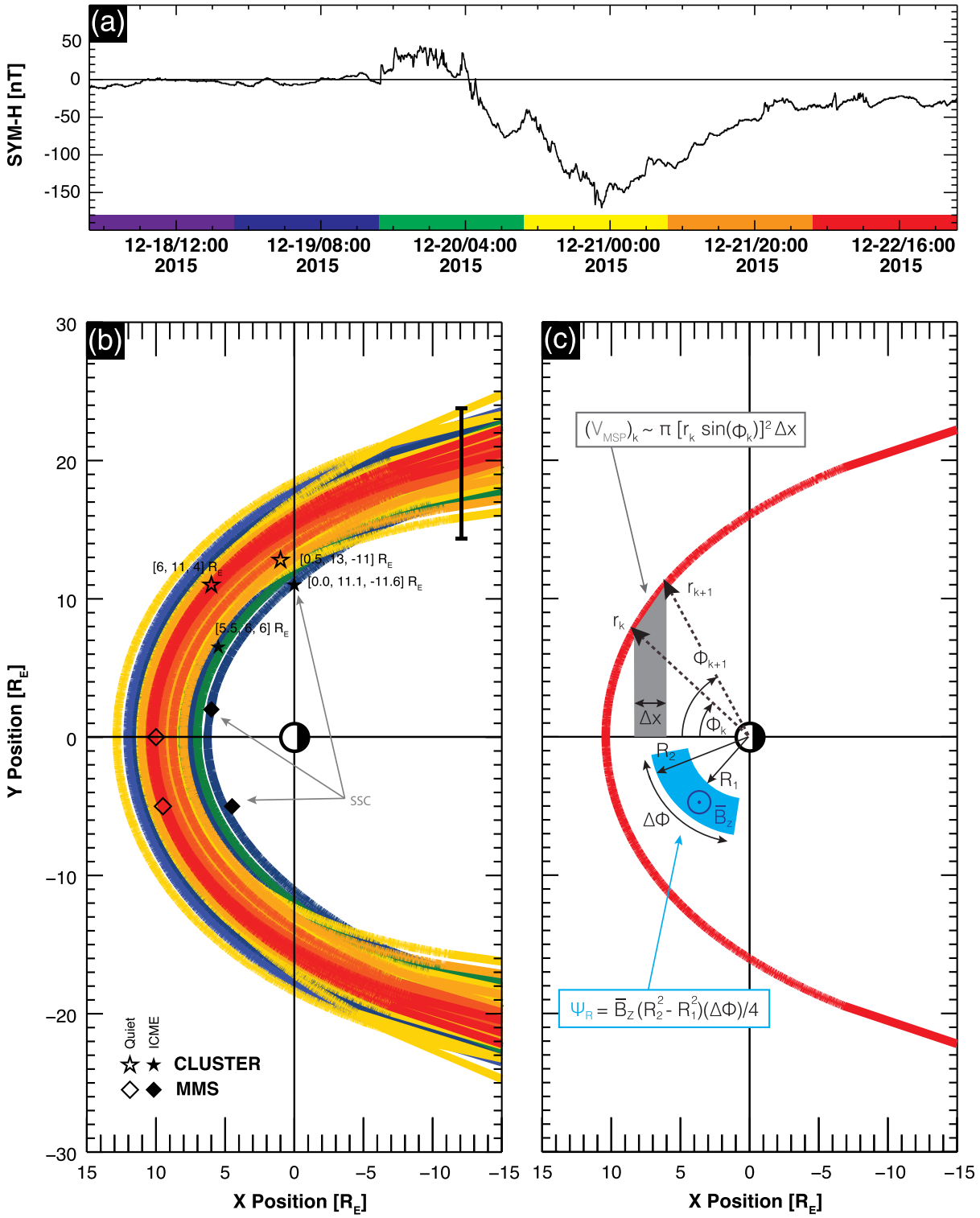

Figure 2. (a) Time series profile of storm-time index SYM-H during ICME 2 (18–29 December 2015), (b) the Shue magnetopause standoff distance model in the GSE *XY* plane for the duration of ICME 2. The colored curves indicate the magnetopause boundary based on the observed OMNI measurements in the solar wind. The shadings of the colored curves correspond to the intervals in panel (a) within which the Shue magnetopause standoff distances were derived. The MMS (diamond) and Cluster (star) magnetopause crossings are provided to validate the model results before (transparent) and during (black) ICME 2. The GSE coordinates of the Cluster MP crossings are also included, and (c) the schematic illustrating the cross section (in gray) of infinitesimally thin disks to determine the Shue model magnetospheric volume V_{MSP}. The schematic also illustrates the radial bins (in cyan) within which average out-of-plane "closed" magnetic field is derived to determine magnetic flux content.

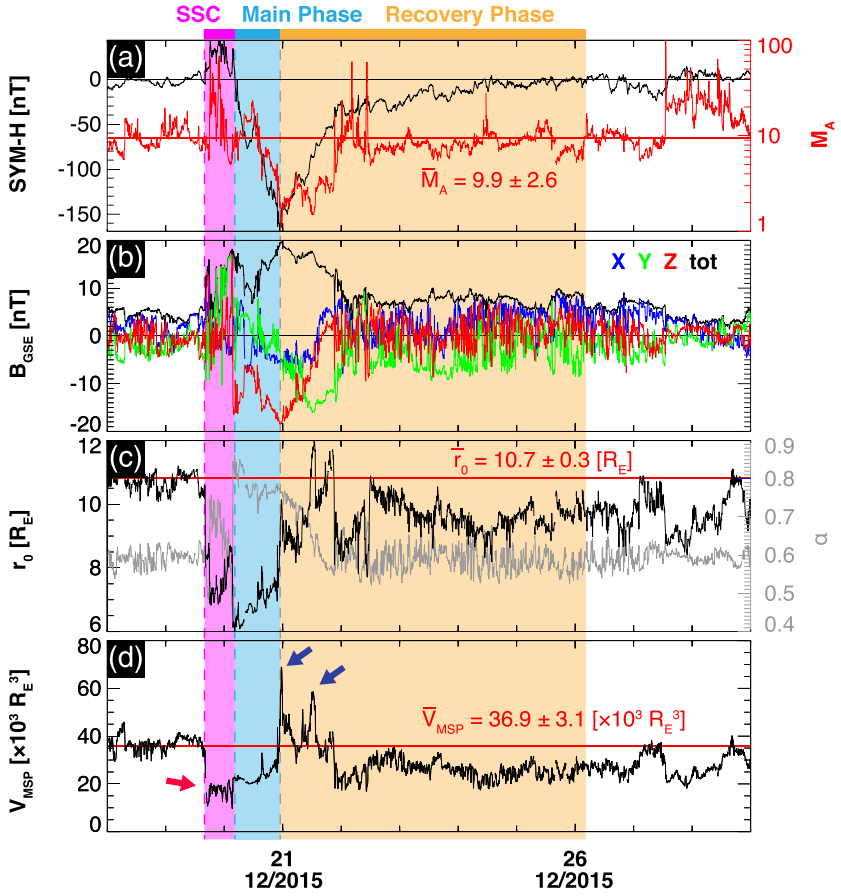

Figure 3. Time series profiles of storm-time (a) SYM-H and IMF M_A (red), (b) IMF B in GSE coordinates, (c) the Shue model magnetopause standoff distance r_0 (black) and tail flaring α (gray), and (d) the Shue model magnetospheric volume V_{MSP} between $-15 < X\ [R_E] < r_0$. The solid red lines indicate the average value before ICME arrival (18 December 2015, 00:00 UT to 19 December 2015, 11:00 UT). The storm intervals are marked with magenta (SSC), cyan (main phase), and orange (recovery phase) shades.

statistical fit to magnetopause crossings at similar solar wind conditions. The empirical Shue magnetopause model does not describe dynamical features such as magnetopause erosion and local time asymmetries and may not be accurate during extreme events.

In Figure 2b, the diamond-shaped markers show the near-equatorial MMS magnetic field measurements (Russell et al., 2016) of magnetopause crossings before (Quiet; unshaded) and during (ICME; black shade) the ICME 2 arrival. Moreover, the star-shaped markers represent the near-polar Cluster observations of magnetopause crossings before and after the ICME 2 arrival, using the onboard magnetic field measurements (Balogh et al., 2001).

Figures 3a–3c provide time series profiles of storm-time (a) SYM-H and IMF M_A, (b) IMF B in GSE coordinates, and (c) the modeled magnetopause standoff distance r_0 and tail flaring α. The solid red lines indicate the average value before ICME 2 arrival (18 December 2015, 00:00 UT to 19 December 2015, 11:00 UT). SYM-H and Alfvénic Mach number were moderately correlated. The sample covariance and correlation for SYM-H and log (M_A) are σ~+6.2 [nT] and ρ~0.7, respectively. Positive covariance ($\sigma > 0$) indicates positive correlation and $\rho = 1$ for perfect correlation.

With increasing upstream dynamic pressure under southward B_z condition, the magnetopause standoff distance was compressed down to geosynchronous orbit, $r < 6.6$ Earth radii. As shown in Figure 3c, the magnetopause standoff distance reduced from 10.7 R_E before the ICME arrival to 8.0 R_E within 10 min at an average rate of −10.8 R_E/hr or −19.1 km/s. The average Alfvén speed inside the dayside magnetosphere is 500–1,000 km/s (Kim et al., 2018).

The compression proceeded during the SSC phase until $r = 6.0$ R_E. With the start of the storm main phase (at 20 December 2015, 04:30 UT), the magnetopause standoff distance started to increase slowly. The magnetopause standoff distance recovery started with the rotation of IMF B_z, at which point IMF B_z becomes and remains southward. The magnetopause standoff distance increased throughout the storm main phase and recovery phase (20 December 2015, 04:30 UT to 21 December 2015, 20:00 UT) at an average rate of $+7.8 \times 10^{-2}$ R_E/hr or +0.16 km/s.

1.3. Storm-Time Magnetospheric Volume

The Shue model magnetopause standoff distance is also used to determine storm-time magnetospheric volume V_{MSP}, defined as $-15 < X\,[R_E] < r_0$, while assuming cylindrical symmetry:

$$V_{MSP}\left[R_E{}^3\right] = \int_{X_1}^{X_2} dx \int_{\theta_1}^{\theta_2} d\phi \int_{R_1}^{R_2} \rho\, d\rho = \int_{-15\ R_E}^{r_0} dx \int_{-\pi/2}^{\pi/2} d\theta \int_0^r \rho\, d\rho$$
$$\cong \pi \left(\sum_k \left[r_k \sin(\phi_k)\right]^2 x_{k+1} - x_k\right)$$

where θ is the polar angle and r represents the Shue magnetopause standoff distance derived from the OMNI measurements of P_{dyn} and B_z. The integration can be simplified as the summation of infinitesimally thin ($\Delta x \rightarrow 0$) disks of radius $\rho(\phi) = r \sin(\phi)$ along the magnetospheric rotation axis X_{GSE}. Figure 2c depicts the cross section of a gray-shaded trapezoid whose sides are functions of ϕ_k and r_k for an arbitrary magnetopause shape, shown as a solid red curve. The gray trapezoid has a width Δx. In the summation notation, $x_k \in [-15, r_0]$ R_E and ϕ_k and r_k refer to the corresponding k^{th} observation. The trapezoid is rotated around X_{GSM} ($\theta = 2\pi$) to form a disk of radius $\rho(\phi_k)$.

Magnetospheric volume is found to reduce significantly with the arrival of ICME 2. Figure 3d represents the time series profile of the modeled magnetospheric volume V_{MSP}. The SSC and storm main phases are marked with magenta and cyan shades, respectively. The pre-storm magnetospheric volume (pre-storm $V_{MSP} = 36.9 \times 10^3$ $R_E{}^3$) sharply reduced, as marked by a red arrow in panel (d), by -20×10^3 $R_E{}^3$ at SSC within 10 min (19 December 2015, 16:07–16:17 UT). The magnetospheric volume continued to drop until reaching a minimum of 10×10^3 $R_E{}^3$ by 19 December 2015, 16:30 UT. At this stage, V_{MSP} remained steadily low at a volume that is 30% of the pre-storm magnetospheric volume.

At the start of the storm main phase (at 20 December 2015, 04:30 UT), IMF became dominantly southward, r_0 sharply decreased to its lowest storm-time distance from the Earth's surface, and V_{MSP} increased. The magnetospheric volume slowly expanded to pre-storm conditions during the storm main phase. At this stage, the magnetopause flaring angle is found to increase and balance the decrease in r_0, resulting in an expanding magnetosphere.

The storm peak (SYM-H < −150 nT; 20 December 2015, 22:15 UT) corresponds to the arrival of the ICME magnetic cloud, where magnetic field magnitude reached $|B_{IMF}| = 20$ nT, IMF was dominantly southward, and solar wind dynamic pressure reduced. Near storm peak, the expanding magnetosphere promptly returns to the pre-storm volume. However, the magnetosphere continued to expand during the recovery phase, marked by the orange-shaded region. In particular, two sharp jumps in V_{MSP}, indicated by blue arrows in panel (d), correspond to the intervals when solar wind flow approached the local Alfvénic velocity, that is, $M_A < 2$. The sample covariance and correlation for $\log(M_A)$ and $\log(V_{MSP})$ are $\sigma \sim -2.3 \times 10^{-2}$ [nT] and $\rho \sim -0.37$, indicating that V_{MSP} and M_A are weakly anticorrelated.

1.4. Storm-Time Dayside "Closed" Magnetic Flux Content

The storm-time compression of the magnetosphere is considered as one of the primary causes of electromagnetic disturbances and therefore is especially important for modern and technologically advanced societies (e.g., Baker, 1996; Winter, 2019). As shown in the previous section, the magnetospheric volume reduced significantly at SSC. Here, we investigate the flux content of "closed" magnetic fields within the dayside magnetosphere before and during SSC, using MMS, GOES 15, and Van Allen Probe (Mauk et al., 2012) magnetic field observations. "Closed" magnetic field lines are rooted in the Earth's iron core through the Northern and Southern magnetic poles.

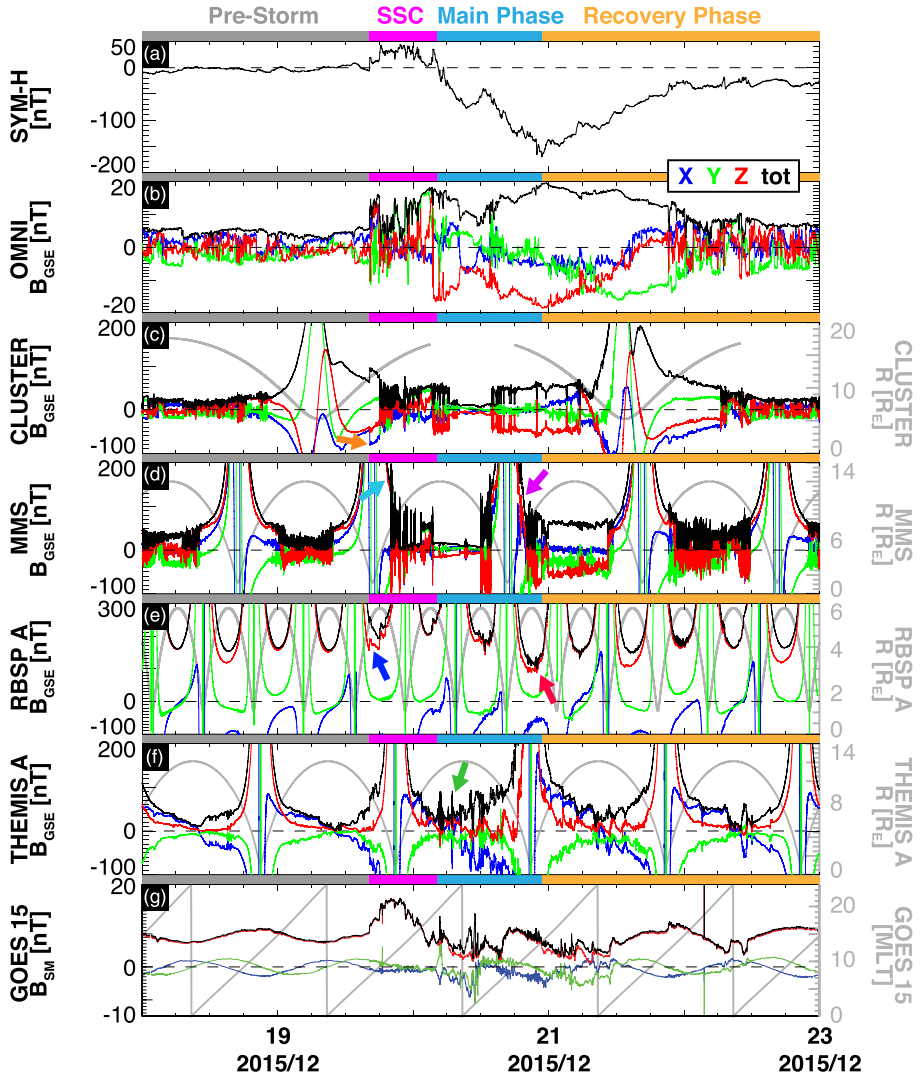

Figure 4. Storm-time in situ measurements for ICME 2 from OMNI, Cluster, MMS, RBSP, THEMIS, and GOES spacecraft. The panels include (a) SYM-H, and magnetic field magnitude and vector in GSE coordinates and trajectory radial distances for (b) OMNI IMF, (c) Cluster 4, (d) MMS4, (e) Van Allen Probe A (RBSP; Kletzing et al., 2013), (f) THEMIS A (Auster et al., 2008), and (g) GOES 15 (Singer et al., 1996) in solar magnetic (SM) coordinates and longitudinal position (MLT) at $R \sim 6.7$ R_E. The spacecraft positions are included in gray on the right y axes. The storm intervals are marked with gray (pre-storm), magenta (SSC), cyan (main phase), and orange (recovery phase) shades.

Figure 4 provides an overview of the pre- and post-SSC magnetic field measurements inside and upstream of the magnetosphere from OMNI, Cluster, MMS, Van Allen Probes (RBSP), THEMIS (Angelopoulos, 2008), and GOES 15 data sets. The panels from top to bottom include (a) SYM-H, and magnetic field magnitude and vector in GSE coordinates and trajectory radial distances for (b) OMNI IMF, (c) Cluster 4, (d) MMS4, (e) Van Allen Probe A (RBSP; Kletzing et al., 2013), (f) THEMIS A (Auster et al., 2008), and (g) GOES 15 (Singer et al., 1996) in solar magnetic (SM) coordinates and longitudinal position (MLT) at $R \sim 6.7$ R_E. The equatorial and meridional trajectory projections for each spacecraft are provided in Figure 5 for 19 December 2015, 00:00–23:59 UT. The modeled magnetopause and shock boundaries are provided for low ($P_{dyn} = 2$ nPa; dashed gray curves) and high ($P_{dyn} = 20$ nPa; solid black curves) upstream dynamic pressures.

The Cluster spacecraft were on an outbound trajectory when ICME 2 arrived on 19 December 2015. At SSC, the B_x component nearly doubled in closed plasma sheet fields at the location of Cluster 4, $\boldsymbol{r}_{C4} = [-3.3, 2.8, -10.7]$ R_E GSE, indicating the compression of the closed field region in the magnetotail. The B_x jump is

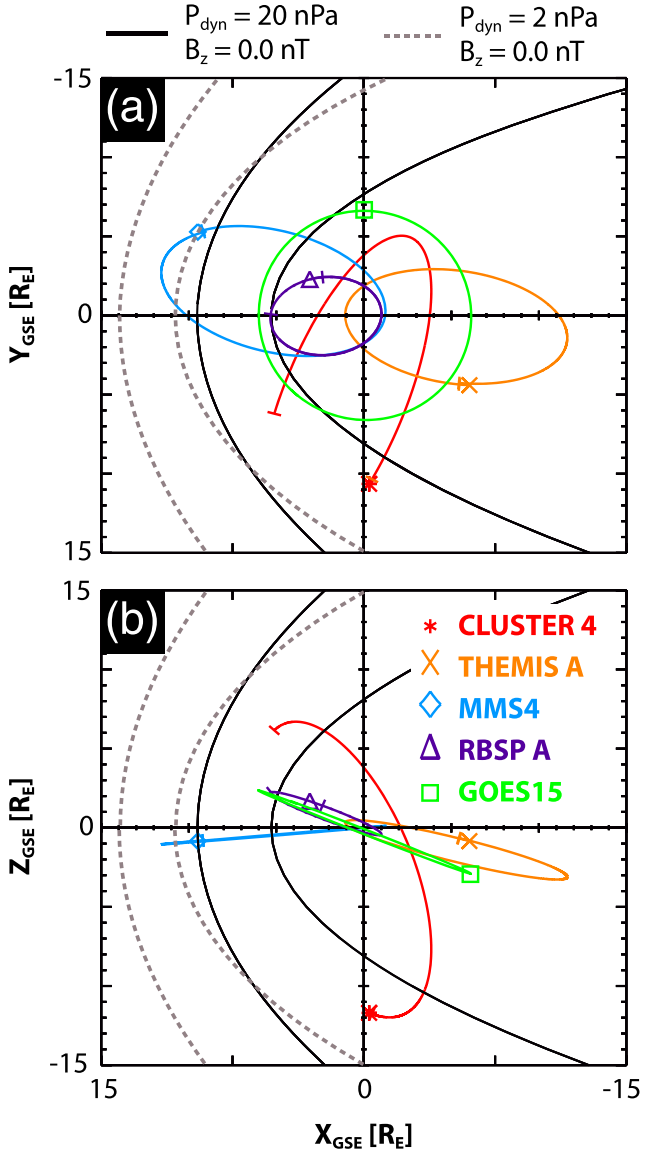

Figure 5. The spacecraft trajectory projections for 19 December 2015, 00:00–23:59 UT in the GSE *XY* and *XZ* planes. The modeled magnetopause and shock boundaries are provided for low (P_{dyn} = 2 nPa; dashed gray curves) and high (P_{dyn} = 20 nPa; solid black curves) upstream dynamic pressures.

marked by an orange arrow in panel (c). At 20 December 2015, 01:00 UT, Cluster 4 crossed the magnetopause at [−0.0, 11.1, −11.6] R_E GSE and entered the magnetosheath. Similarly, the MMS spacecraft were located in the magnetosphere before SSC. During SSC, MMS4 crossed the magnetopause at [4.6, −5.3, −0.4] R_E GSE on its outbound trajectory at 20:00 UT. The storm-time magnetopause crossing by MMS is marked by a cyan arrow in panel (d). SSC was also detected by RBSP A. At the time of ICME shock arrival, RBSP A was positioned in the dayside inner magnetosphere at [4.3, −1.7, 2.1] R_E GSE. The impact resulted in a sudden 20% increase in B_z, as indicated by a blue arrow in panel (e). Lastly, THEMIS A also detected the storm arrival while in the magnetotail [−8.0, −2.2, −2.8] R_E GSE. The near-Earth magnetotail reconnection event of 20 December 2015, reported by Angelopoulos et al. (2020), is marked by a green arrow in panel (f). Enhanced dipolarization fronts are also observed in the vicinity of the reconnection site. Similar magnetic signatures are observed closer to Earth in GOES 15 observations.

Next, the magnetic flux content in the dayside magnetosphere, defined as $-\frac{\pi}{2} \le \phi \le +\frac{\pi}{2}$, is determined, assuming cylindrical symmetry:

$$\Psi\ [\text{kilo} - \text{Webers}] = \sum_{R=2}^{10} (\Psi_R) = \sum_{R=2}^{10} \left(\pi\, \overline{B_z} \int_{-\frac{\pi}{2}}^{+\frac{\pi}{2}} d\phi \int_{R}^{R+1} r\, dr \right)$$

where R is the radial distance from the Earth's surface and $\overline{B_z}$ represents the average B_z inside each radial bin. The cyan-shaded region in Figure 2c depicts a radial bin within which the average out-of-plane, "closed" magnetic field, defined as $\overline{B_z} = \frac{1}{N} \sum (B_z]_R^{R+1}]_{-\pi/2}^{\pi/2})$, is determined. N denotes the number of observed data points in each bin. The assumption is that all magnetospheric field lines on the dayside must cross the equatorial plane ($B_Z > 0$ at $Z = 0$ plane). It is also assumed that B_Z is symmetric within each radial bin, $R \in [0,r]$ and $\phi \in [-\pi/2, \pi/2]$. It is assumed that the observed B_z by near-equatorial satellites (MMS and RBSP) are, to a first-order approximation, representative of B_z at the equator. Evidence for the validity of this assumption is provided in Appendix A.

Figure 6 shows the magnetic flux content inside each radial bin Ψ_R before ICME 2 ("Quiet"; blue, 18 December 2015, 10:30–22:50 UT), at SSC ("SSC"; red, 19 December 2015, 16:15–23:50 UT), and at storm main phase peak ("Peak"; green, 20 December 2015, 13:45–22:50 UT) from the RBSP A ($2 \le R\ [R_E] < 6$), GOES 15 ($6 \le R\ [R_E] < 7$), and MMS4 ($7 \le R\ [R_E] < 10$) magnetic field measurements. The error bars indicate the standard deviation of B_z within each radial bin. Spacecraft trajectory radii shown in gray in Figure 4 demonstrate the intervals within which magnetic field data are used for different storm phases.

Interestingly, though expected, we find that magnetic flux content remains constant at SSC while the magnetosphere was compressed under enhanced dynamic pressure and northward B_z conditions. Figure 6 shows that compared to the pre-storm period ($\Psi_R > 9$ kWb for $2 \le R\ [R_E] < 11$), at SSC the magnetosphere was compressed inward (negligible Ψ_R for $R > 6$ R_E). However, magnetic flux was greater in the compressed regions, offsetting the lack of flux at higher R. Finally, the total magnetic flux content was $\sum \Psi_R \sim 170 \pm 30$ kWb for both pre-storm and SSC intervals, indicating that dayside magnetic flux content remained constant at SSC.

In contrast, inside the magnetic cloud, wherein P_{dyn}, β, and M_A are sharply reduced and IMF B was dominantly southward ($B_z < 0$), "closed" magnetic flux content within the dayside magnetosphere does not remain constant. Figure 6 shows that in comparison with the pre-storm period ($\Psi_R > 5$ kWb for $2 \le R$

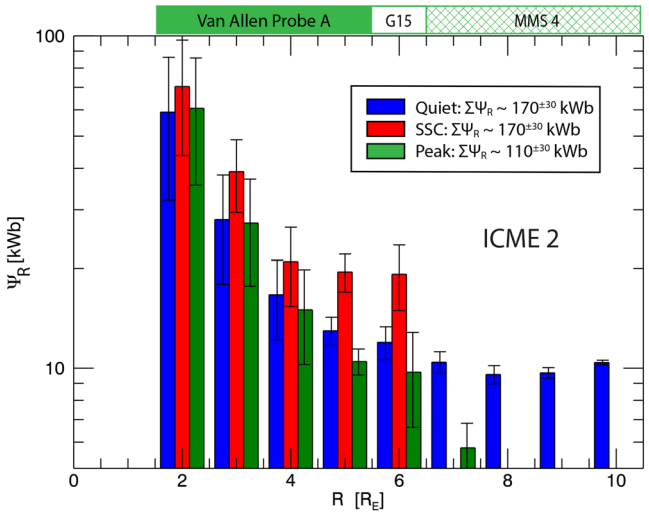

Figure 6. The magnetic flux content inside each radial bin Ψ_R before ICME 2 ("Quiet"; blue, 18 December 2015, 10:30–22:50 UT), at SSC ("SSC"; red, 19 December 2015, 16:15–23:50 UT), and at peak SYM-H ("Peak"; green, 20 December 2015, 13:45–22:50 UT) from the RBSP A ($2 \le R$ [R_E] < 6), GOES 15 ($6 \le R$ [R_E] < 7), and MMS4 ($7 \le R$ [R_E] < 10) magnetic field measurements. The total magnetic flux content $\sum\Psi_R$ in the dayside magnetosphere is included for $2 \le R$ [R_E] < 10.

[R_E] < 11), at storm peak the magnetosphere is compressed inward (negligible Ψ_R for $R > 7$ R_E). The MMS4 and RBSP A magnetospheric conditions at storm peak are marked by magenta and red arrows in Figures 4d and 4f. However, unlike the SSC interval discussed above, at the storm peak the total magnetic flux content in the dayside magnetosphere has decreased by nearly 35% to $\sum\Psi_R$~110 ± 30 kWb, indicating magnetospheric erosion during the magnetic cloud encounter, especially at $R \ge 5$ R_E. As discussed in the next section, different dayside and nightside reconnection rates and therefore the different rates at which magnetic flux is transported and recycled by the Dungey cycle may explain this dayside flux erosion. Another possible, though less explored, scenario involves "closed" magnetic flux disconnecting from the magnetosphere at the time when IMF reconnects with magnetospheric fields at multiple sites along the dayside magnetopause (Øieroset et al., 2019; Russell & Qi, 2020).

2. Storm-Time Flux Transport

Signatures of dayside magnetic flux erosion, that is, magnetic reconnection, and tailward flux transport were observed during the SSC phase. In particular, during the encounter with the ICME 2 sheath region, the MMS spacecraft detected reconnected magnetic flux at the magnetopause transported tailward as bundles of "open" magnetic flux tubes with a flux rope-like geometry, known as flux transfer events (FTEs) (e.g., Akhavan-Tafti, Slavin, Eastwood, et al., 2019; Akhavan-Tafti, Slavin, Sun, et al., 2019; Akhavan-Tafti et al., 2020; Russell & Elphic, 1979). Figure 7a shows the close-up view of the magnetic signatures inside and surrounding the FTE in the turbulent magnetosheath behind the quasi-parallel bow shock (e.g., Pollock et al., 2018). The FTE is also marked by a black arrow in Figure 4d. Figures 7b and 7c provide the results from applying the minimum variance analysis (MVA; Sonnerup & Scheible, 1998; Xiao et al., 2004) on magnetic field signatures within 19 December 2015, 20:35:10–20:54:50 UT. The results indicate, as expected for an FTE-type flux rope, a rotation in the magnetic field. They also indicate that the FTE axis (MVA intermediate eigenvector) is mainly oriented along the *XY* plane (Wang et al., 2006), corresponding to enhanced IMF B_y. Supporting Information Figure S1 further shows the Geotail magnetic and plasma observations in the solar wind.

The FTE is observed at SSC when the magnetopause was compressed at a radial distance 8 R_E and contains significant magnetic flux. The FTE corresponds to a time of enhanced IMF B_y and reduced dynamic pressure. The FTE core magnetic field strength B_A reaches 90 nT. The FTE is found to convect (not shown here) at velocity $\boldsymbol{v}_{FTE} = 75$ [km/s] × [−0.71, −0.71, 0] GSE. This corresponds to an estimated FTE radius $r_{FTE} \sim 3.7$ R_E and magnetic flux content $\Psi_{FTE} \sim \pi (r_{FTE})^2 B_A = 160$ MWb, assuming circular cross section. The FTE dimensions are comparable to the previously reported FTEs at low-latitude flanks. However, the magnetic flux content of this FTE is more than 2 orders of magnitude larger than that reported by Eastwood et al. (2012) (<2 MWb), due to its strong core field strength in close proximity to inner magnetosphere. This magnetic flux content is comparable to the estimated total reconnected magnetic flux in the magnetotail during the same ICME encounter (~0.2 GWb; Angelopoulos et al., 2020), marked with a green arrow in Figure 4f.

3. Discussion

A clear understanding of storm-time magnetospheric dynamics is essential for improving the space weather forecasting and mitigation procedures. The main objectives of the present study are to (1) provide an overview of the role of various ICME physical properties and their geoeffectiveness, (2) investigate the magnetopause standoff distance and the estimated magnetospheric volume under different storm-time intervals, and (3) quantify the magnetospheric magnetic flux content under different storm-time intervals. These are made possible by the host of satellites sampling the solar wind and the Earth's inner and outer magnetospheres simultaneously. Our cross-scale examination of the magnetosphere sheds light on the sources and the temporal evolution of storm-time magnetospheric dynamics.

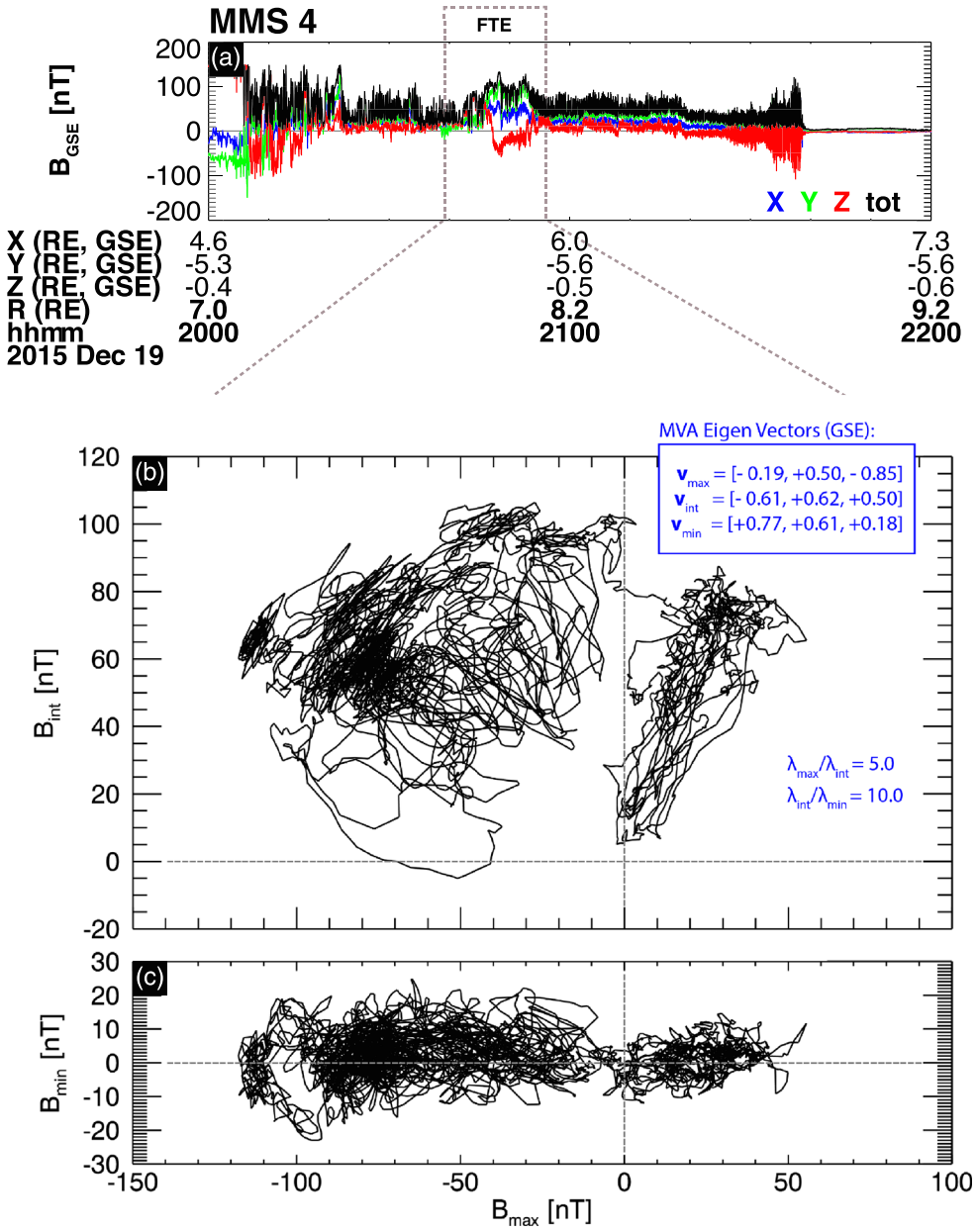

Figure 7. (a) The MMS4 magnetic measurements inside and surrounding an FTE in GSE coordinates. Minimum variance analysis (MVA) applied on magnetic field on magnetic field signatures within 19 December 2015, 20:35:10–20:54:50 UT. The panels include (b) maximum (max) and intermediate (int) components of the magnetic field, and (c) maximum (max) and minimum (min) components of the magnetic field. The MVA eigenvectors in GSE coordinates and eigenvalue ratios are included.

We found that the magnetosphere is compressed during the SSC interval (SYM-H > 0), when dynamic pressure in the ICME sheath region is enhanced and the dawn-dusk component of IMF B is dominant. At SSC, the magnetopause standoff distance compression commences at a fast rate of ~−10.8 R_E/hr. After the SSC, the compression proceeds, though slower, until IMF B becomes dominantly southward ($B_z < 0$). The southward rotation of IMF starts the storm main phase during which SYM-H becomes more negative. We found that the magnetopause standoff distance starts to recover to pre-storm conditions at a slow rate of $+7.8 \times 10^{-2}$ R_E/hr during the storm main phase and recovery phase, even though |SYM-H| continues to increase until reaching a peak. Similarly, magnetospheric volume was found to reduce sharply by nearly

40% at the ICME shock encounter. The magnetospheric volume reaches a minimum ($V_{MSP,\ SSC} < 30\%\ V_{MSP,\ pre\text{-}ICME}$), when interacting with the ICME sheath, before the start of the storm main phase. Though the magnetospheric volume recovered by the end of the storm main phase, the magnetosphere continued to expand sunward in the early part of the recovery phase when still located inside the magnetic could ($M_A < 2$). It is important to note that V_{MSP} assumes cylindrical symmetry and does not take into account complex geometries at the northern and southern cusps.

The variations in the magnetopause standoff distance and, therefore, the magnetospheric volume directly impact the magnetic flux content in the magnetosphere. Here, we investigated the storm-time "closed" magnetic flux content within the dayside magnetosphere, using in situ MMS, GOES 15, and Van Allen Probe magnetic field measurements. We found that "closed" magnetic flux remained constant during the SSC interval (SYM-H > 0), when dynamic pressure in the ICME sheath region was enhanced and the dawn-dusk component of IMF B was dominant. The storm-time magnetospheric compression due to the enhanced dynamic pressure resulted in the rearrangement of magnetic fields in the dayside magnetosphere.

A large FTE was observed during the SSC phase, indicating the occurrence of dayside magnetic reconnection (e.g., Akhavan-Tafti et al., 2020). The FTE contained nearly 160 MWb, much larger than other FTE observations (e.g., Wang et al., 2006). The dayside magnetic reconnection opens "closed" magnetospheric field lines, resulting in a bundle of "opened" field lines that can form FTE-type flux ropes. FTEs are connected to the ionosphere on one side and to the solar wind on the other end. This FTEs' "opened" magnetic flux content is comparable to the estimated total reconnected magnetic flux, also known as "flux closure," in the magnetotail during the same ICME encounter (~0.2 GWb), as reported by Angelopoulos et al. (2020). The dayside reconnection rate is governed by IMF orientation and solar wind plasma properties, while nightside reconnection is controlled by magnetotail conditions (Torbert et al., 2018). Conditions in the magnetotail are influenced by the dayside reconnection rate, such as via loading of the magnetospheric lobes with open flux during southward IMF. Our observations suggest that, during the SSC phase, the magnetic flux opened by the dayside reconnection, as indicated by the FTE, caused a magnetotail reconnection with comparable reconnection rate, resulting in the observed "closed" magnetic flux remaining constant at SSC.

5On the contrary, at the storm main phase and peak, when located inside the magnetic cloud wherein IMF B_z was dominant and southward and $\beta < 0.1$ and $M_A \sim 1.0$, the dayside magnetosphere expanded. At this stage, it was found that magnetic flux does not remain constant. In fact, the magnetosphere contains 35% less magnetic flux within $2 \leq R\ [\mathrm{R_E}] < 11$ than pre-storm (and SSC) conditions. This suggests that the magnetospheric "closed" magnetic field must be eroded during the magnetospheric re-expansion period, without immediate replacement by magnetotail reconnection and Earthward convection. The magnetospheric magnetic flux erosion was most significant at $R \geq 5\ \mathrm{R_E}$. This "SSC" to "Peak" reduction in magnetic flux over nearly 13 hr is equivalent to a potential $\varnothing = \frac{\Delta\Psi}{\Delta t} = \frac{-60\ \mathrm{kWb}}{13\ \mathrm{hr}} = 1.3$ kWb/s or V (e.g., Stephens et al., 2016).

In other words, at the storm main phase and peak, the nightside reconnection rate did not instantaneously readjust itself to changes in the dayside rate. Therefore, the time lag between the dayside and nightside reconnections caused erosion in "closed" magnetic flux at $R \geq 5\ \mathrm{R_E}$. This can result in the expansion of the polar cap, defined as the boundary between open and closed magnetospheric fields (e.g., Russell, 1972). Future studies will investigate the relationship between storm-time closed magnetic flux content and the polar cap size and potential (Milan et al., 2007). Storm-time relative magnetopause and magnetotail reconnection rates shall also be determined.

ICME-driven storms cause drastic variation in outer radiation belt electrons (e.g., Turner et al., 2019). The storm-time magnetopause compression at SSC can lead to the loss of magnetospheric trapped plasma population. The trapped radiation belt electrons are known to be lost to the magnetopause, via a process known as "magnetopause shadowing" and outward radial transport (e.g., Ukhorskiy et al., 2006). The magnetopause shadowing involves the inward motion of the magnetopause due to the enhanced storm-time dynamic pressure. This inward magnetopause motion results in the intensification of the ring current, as indicated by the enhancing storm-time index, SYM-H. This leads to the expansion of electron drift orbits such that their paths intersect the magnetopause leading to rapid electron losses. Turner et al. (2012) also attributed the sudden

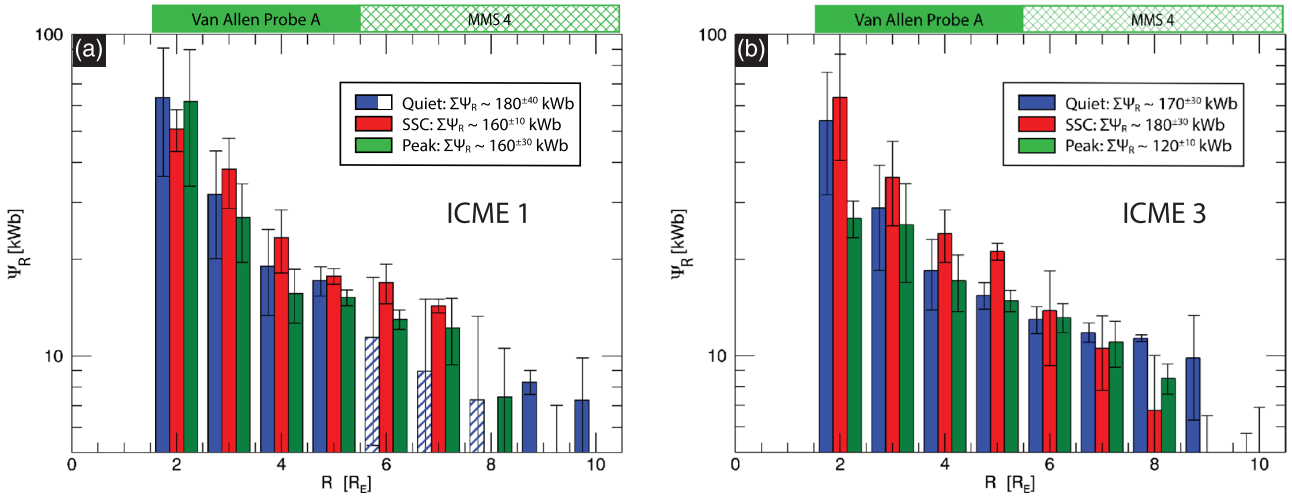

Figure 8. The magnetic flux content inside each radial bin Ψ_R before (a) ICME 1 ("Quiet"; blue, 13 December 2015, 23:30 UT to 14 December 2015, 12:00 UT), at SSC ("SSC"; red, 14 December 2015, 13:30–14:30 UT), and at peak SYM-H ("Peak"; green, 14 December 2015, 16:50–22:40 UT) and (b) ICME 3 ("Quiet"; blue, 30 December 2015, 09:15–18:20 UT), at SSC ("SSC"; red, 31 December 2015, 03:00–13:00 UT), and at peak SYM-H ("Peak"; green, 31 December 2015, 13:00–20:00 UT) from the RBSP A ($2 \le R\ [R_E] < 6$) and MMS4 ($6 \le R\ [R_E] < 10$) magnetic field measurements. The total magnetic flux content $\sum\Psi_R$ in the dayside magnetosphere is included for $2 \le R\ [R_E] < 10$. The SSC magnetic flux content was extrapolated in ICME 1 for $6 \le R\ [R_E] < 9$, since the MMS spacecraft were near their perigee just before SSC, as indicated by dashed blue bars. Magnetic flux content for these radial distances is extrapolated from a power law fit to MMS and RBSP observations at other radial distances: $f(x) = a\ x^b$, where coefficients $a = 183$ (143.4, 222.6) and $b = -1.549$ (−1.779, −1.319). The values in parentheses indicate the 95% confidence bounds.

loss of radiation belt electrons to their outward transport during the main phase of a storm. Future investigations will examine the temporal evolutions of storm-time magnetospheric plasma energization and loss mechanisms (e.g., Goldstein et al., 2017).

4. Comparative Analysis

As described above, ICME 2 was one of a chain of three independent and well-separated ICMEs spanning 1 month (12 December 2015 to 12 January 2016). All three ICMEs are composed of a shock, sheath, and magnetic cloud regions. As listed in Table 1, the magnetic cloud scale sizes were estimated to range between 1,500 and 8,000 R_E (i.e., ~0.06 to 0.34 AU). At the closest approach, the magnetic field magnitude inside the magnetic clouds reached 15–20 nT, which are >3 times the average IMF magnitude. Plasma dynamic pressure peaked within the sheath regions following the shocks. Storm-time index reached SYM-H < −150 nT. The ICME geoeffectiveness directly correlated with the ratios of plasma beta and Alfvénic Mach number of the ICME sheath to magnetic cloud. In particular, the ratios $\frac{\beta_{SH}}{\beta_{MC}} \sim 200$ and $\frac{M_{A,\,SH}}{M_{A,\,MC}} \sim 10$ were observed during ICME 2 which was the most geoeffective (SYM-H < −150 nT) of the three ICMEs.

The dayside "closed" magnetic flux content was found to remain constant during ICME 2 SSC phase and reduce by 35% at storm main phase. Here, we further investigate closed magnetic flux content during storm phases for ICMEs 1 and 3. The radial profiles of the dayside closed magnetospheric magnetic flux contents for ICME 1 and ICME 3 are included in Figures 8a and 8b. Similar to Figure 6, the total closed magnetic flux content is determined inside each radial bin Ψ_R before, during, and at ICME 1 and ICME 3 SYM-H peak from the RBSP A ($2 \le R\ [R_E] < 6$) and MMS4 ($6 \le R\ [R_E] < 10$) magnetic field measurements. Table 2 summarizes the total magnetic flux content $\sum\Psi_R$ within radial distances $2 \le R\ [R_E] < 10$ during different storm intervals for the three ICMEs. No MMS observations were available for $6 \le R\ [R_E] < 9$ for this period, since the MMS spacecraft were near their perigee just before SSC. Therefore, magnetic flux content for these radial distances is extrapolated from a power law fit to MMS and RBSP observations at other radial distances: $f(x) = a\ x^b$, where coefficients $a = 183$ (143.4, 222.6) and $b = -1.549$ (−1.779, −1.319). The values in parentheses indicate the 95% confidence bounds.

Table 2
The Total Magnetic Flux Content $\sum\Psi_R$ Within Radial Distances $2 \le R$ [R_E] < 10 During Different Storm Intervals for the Three ICMEs

	Pre-storm[a] [kWb]	SSC[b] [kWb]	Peak[c] [kWb]
ICME 1	180 ± 40[d]	160 ± 10	160 ± 10
ICME 2	170 ± 30	170 ± 30	110 ± 30
ICME 3	170 ± 30	180 ± 30	120 ± 10

[a]"Pre-storm" refers to values collected during one complete RBSP orbit before SSC. [b]"SSC" refers to values collected during one RBSP orbit during SSC (SYM-H > 0 [nT]). [c]"Peak" refers to values collected during one RBSP orbit during storm main phase, including the storm peak where SYM-H reaches its lowest value. [d]No MMS observations were available for $6 \le R$ [R_E] < 9 for this period, since the MMS spacecraft were near their perigee just before SSC. Therefore, magnetic flux content for these radial distances is extrapolated from a power law fit to MMS and RBSP observations at other radial distances: $f(x) = a\ x^b$, where coefficients $a = 183$ (143.4, 222.6) and $b = -1.549$ (−1.779, −1.319). The values in parentheses indicate the 95% confidence bounds.

The net dayside closed magnetic flux content remains constant in SSC phase in all three ICMEs. In contrast, magnetic flux is reduced by nearly 30% in storm main phase in ICME 3, similar to ICME 2. The closed magnetic flux content did not change significantly in ICME 1 storm main phase. This can be further linked to the ICMEs' SYM-H profiles. ICME 1 main phase appeared as a smooth decrease in SYM-H before recovering. Unlike ICME 1, ICMEs 2 and 3 showed double-dip SYM-H signatures during the main phases (first dip from sheath and second dip from the magnetic cloud). Future investigations will examine the relationship between SYM-H profile and the variations in storm-time dayside closed magnetic flux content.

Lastly, the storm-time interplanetary conditions at Earth are at times similar to the environment in close proximity to the Sun. In particular, plasma beta and the Alfvénic Mach number are found to reduce significantly inside the magnetic cloud ($\beta < 0.1$ and $M_A \sim 1.0$). For comparison, at Mercury where the average radial distance from the Sun is ~0.4 AU, the average $M_A \sim 6.6$ (Winslow et al., 2013). Slavin et al. (2012) showed, using MErcury Surface, Space ENvironment, GEochemistry, and Ranging (MESSENGER) measurements, that magnetopause reconnection played a dominant role in driving the magnetospheric convection at Mercury. In particular, the authors discovered that more than 50% of the reconnected magnetic flux at the magnetopause was transported tailward as FTEs. Similarly, enhanced ion-scale FTE counts were reported during Mercury's disappearing dayside magnetosphere under extreme solar wind conditions, defined as solar wind dynamic pressure $P_{dyn} > 140$ nPa (Slavin et al., 2019). In contrast, at Earth, the average contribution of FTEs (average diameter $d \sim 1$ R_E and magnetic flux content $\psi \sim 1$ MWb; Akhavan-Tafti et al., 2018) to the magnetospheric convection has been estimated at ~0.1% (e.g., Rijnbeek et al., 1984). However, in this study, we provided evidence for one large-scale FTE that transported up to 160-MWb magnetic flux to the magnetotail during SSC. Future analyses will explore storm-time magnetic reconnection signatures near the dayside geosynchronous region and investigate the prevalence of FTEs and their size distribution at Earth under low-M_A conditions.

5. Conclusion

In conclusion, a clear understanding of storm-time magnetospheric dynamics is essential for improving space weather forecasting and mitigation procedures. In this study, cross-scale observations of storm-time magnetospheric dynamics during a chain of three independent and well-separated ICME events were presented. It was found that the subsolar magnetopause standoff distance moved planetward at a rate ~−10.8 R_E/day at the SSC phase. This inward motion continued until reaching geosynchronous orbit resulting in a 70% decrease in pre-storm magnetospheric volume. The dayside closed magnetic flux content is quantified using in situ OMNI, Geotail, Cluster, MMS, GOES, Van Allen Probes, and THEMIS measurements at different radial distances. It was shown that the total magnetic flux remained constant within the compressed and reconnecting dayside magnetospheric region. In contrast, the dayside magnetospheric magnetic flux does not remain constant at storm main phase and peak when the magnetospheric volume increased while IMF was dominantly southward, indicating magnetic flux erosion at the dayside magnetopause. The magnetospheric magnetic flux erosion especially impacted the magnetic environment at radial distances $R \ge 5$ R_E. It is concluded that a time lag in storm-time Dungey cycle resulted in inadequate replenishment of the eroded dayside magnetospheric flux which can lead to enhanced plasma transport through the magnetopause during increased solar wind activity.

Appendix A: Testing the Validity of the Methodology

There are two possible approaches to address the Heliophysics System Observatory's (HSO) lack of multi-scale equatorial fields measurements. One approach is to map non-equatorial magnetic field observations to the equator using empirical magnetospheric models (Tsyganenko & Sitnov, 2007) or to assume that near-equatorial B_z (within a relative small distance from the equatorial plane) is comparable to that at the

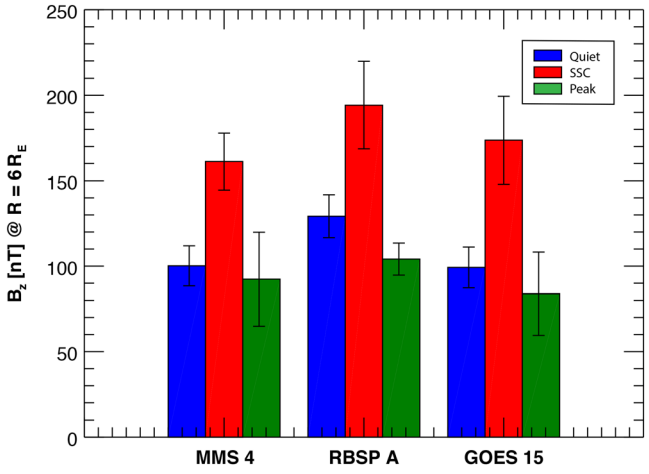

Figure A1. The juxtaposition of the observed B_z inside radial bin $R = 6$ R_E before ICME 2 ("Quiet"; blue, 18 December 2015, 10:30–22:50 UT), at SSC ("SSC"; red, 19 December 2015, 16:15–23:50 UT), and at peak SYM-H ("Peak"; green, 20 December 2015, 13:45–22:50 UT) from RBSP A, GOES 15, and MMS4. The relative standard deviation (RSD) of B_z between observations at different distances from the equator is RSD < 15%. This RSD is comparable to that of total fluxes in Figures 6 and 8.

equator. Each approach presents a set of advantages and caveats, in particular with regard to reliability under extreme space weather conditions.

In this study, it is assumed that the observed B_z by near-equatorial spacecraft (MMS and RBSP) are, to a first-order approximation, representative of B_z at the equator (GOES). To test the validity of this assumption, the observed B_z in bin $R = 6$ R_E is compared between the three spacecraft. The bin $R = 6$ R_E is selected since it is the bin within which the three orbits overlap. GOES is on an equatorial orbit, while MMS and RBSP orbits are near-equatorial, with inclination angles 28° and 10°, respectively.

Figure A1 shows the average B_z within the radial bin $R = 6$ R_E by MMS4, RBSP A, and GOES 15 during the ICME 2 encounter. The observations are compared between different storm-time conditions. It is indicated that the variation in B_z between the three spacecraft is relatively small, with a relative standard deviation RSD < 15%. It is further found that the assumption remains valid under different space weather conditions. Therefore, it is concluded that the observed B_z by MMS and RBSP spacecraft are, to a first-order approximation, representative of B_z at the equator.

Data Availability Statement

The data included in this study are publicly available at NASA/GSFC's Space Physics Data Facility's CDAWeb (https://cdaweb.gsfc.nasa.gov/index.html/) and OMNIWeb services (https://omniweb.gsfc.nasa.gov/), ESA Cluster Science Archive (https://csa.esac.esa.int/csa-web/), and JAXA DARTS Solar-Terrestrial Physics (https://www.darts.isas.jaxa.jp/stp/geotail/data.html). The Space Physics Environment Data Analysis Software framework (SPEDAS; http://spedas.org/) was used to analyze and plot the data.

Acknowledgments

This work was supported by the DGA project, École Polytechnique, Université Paris-Saclay, convention 2778/IMES. The work done at the University of Michigan was supported by NASA MMS contract NNG04EB99C at the Southwest Research Institute, NASA MMS GI grant 80NSSC18K1363, and NASA grants 80NSSC18K0999, 80NSSC20K1847, and NNN06AA01C.

References

Akasofu, S.-I. (1981). Energy coupling between the solar wind and the magnetosphere. *Space Science Reviews*, *28*(2), 121–190. https://doi.org/10.1007/BF00218810

Akhavan-Tafti, M., Palmroth, M., Slavin, J. A., Battarbee, M., Ganse, U., Grandin, M., et al. (2020). Comparative analysis of the Vlasiator simulations and MMS observations of multiple X-line reconnection and flux transfer events. *Journal of Geophysical Research: Space Physics*, *125*, e2019JA027410. https://doi.org/10.1029/2019JA027410

Akhavan-Tafti, M., Slavin, J. A., Eastwood, J. P., Cassak, P. A., & Gershman, D. J. (2019). MMS multi-point analysis of FTE evolution: Physical characteristics and dynamics. *Journal of Geophysical Research: Space Physics*, *124*, 5376–5395. https://doi.org/10.1029/2018JA026311

Akhavan-Tafti, M., Slavin, J. A., Sun, W. J., Le, G., & Gershman, D. J. (2019). MMS observations of plasma heating associated with FTE growth. *Geophysical Research Letters*, *46*, 12,654–12,664. https://doi.org/10.1029/2019GL084843

Akhavan-Tafti, M., Slavin, J. A. A., Le, G., Eastwood, J. P. P., Strangeway, R. J., Russell, C. T., et al. (2018). MMS examination of FTEs at the Earth's subsolar magnetopause. *Journal of Geophysical Research: Space Physics*, *123*, 1224–1241. https://doi.org/10.1002/2017JA024681

Angelopoulos, V. (2008). The THEMIS mission. *Space Science Reviews*, *141*(1–4), 5–34. https://doi.org/10.1007/s11214-008-9336-1

Angelopoulos, V., Artemyev, A., Phan, T. D., & Miyashita, Y. (2020). Near-Earth magnetotail reconnection powers space storms. *Nature Physics*, *16*, 1–5. https://doi.org/10.1038/s41567-019-0749-4

Auster, H. U., Glassmeier, K. H., Magnes, W., Aydogar, O., Baumjohann, W., Constantinescu, D., et al. (2008). The THEMIS fluxgate magnetometer. *Space Science Reviews*, *141*(1–4), 235–264. https://doi.org/10.1007/s11214-008-9365-9

Baker, D. N. (1996). Solar wind-magnetosphere drivers of space weather. *Journal of Atmospheric and Terrestrial Physics*, *58*(14), 1509–1526. https://doi.org/10.1016/0021-9169(96)00006-2

Baker, D. N. (2000). Effects of the Sun on the Earth's environment. *Journal of Atmospheric and Solar-Terrestrial Physics*, *62*(17–18), 1669–1681. https://doi.org/10.1016/S1364-6826(00)00119-X

Balogh, A., Carr, C. M., Acuna, M. H., Dunlop, M. W., Beek, T. J., Brown, P., et al. (2001). The Cluster Magnetic Field Investigation: Overview of in-flight performance and initial results. *Annales Geophysicae*, *19*. https://doi.org/10.5194/angeo-19-1207-2001

Burch, J. L., Moore, T. E., Torbert, R. B., & Giles, B. L. (2016). Magnetospheric multiscale overview and science objectives. *Space Science Reviews*, *199*(1–4), 5–21. https://doi.org/10.1007/s11214-015-0164-9

Burch, J. L., & Phan, T. D. (2016). Magnetic reconnection at the dayside magnetopause: Advances with MMS. *Geophysical Research Letters*, *43*, 8327–8338. https://doi.org/10.1002/2016GL069787

Burlaga, L. F. (1988). Magnetic clouds and force-free fields with constant alpha. *Journal of Geophysical Research*, *93*(A7), 7217. https://doi.org/10.1029/JA093iA07p07217

Dungey, J. W. (1961). Interplanetary magnetic field and the auroral zones. *Physical Review Letters*, *6*(2), 47–48. https://doi.org/10.1103/PhysRevLett.6.47

Eastwood, J. P., Phan, T. D., Fear, R. C., Sibeck, D. G., Angelopoulos, V., Ieroset, M., & Shay, M. A. (2012). Survival of flux transfer event (FTE) flux ropes far along the tail magnetopause. *Journal of Geophysical Research*, *117*, A08222. https://doi.org/10.1029/2012JA017722

Escoubet, C. P., Schmidt, R., & Goldstein, M. L. (1997). Cluster—science and mission overview. In C. P. Escoubet, C. T. Russell, R. Schmidt (Eds.), *The Cluster and Phoenix missions* (pp. 11–32). Dordrecht: Springer. https://doi.org/10.1007/978-94-011-5666-0_1

Goldstein, J., Angelopoulos, V., De Pascuale, S., Funsten, H. O., Kurth, W. S., LLera, K., et al. (2017). Cross-scale observations of the 2015 St. Patrick's day storm: THEMIS, Van Allen Probes, and TWINS. *Journal of Geophysical Research: Space Physics*, *122*, 368–392. https://doi.org/10.1002/2016JA023173

Gonzalez, W. D., Joselyn, J.-A., Kamide, Y., Kroehl, H. W., Rostoker, G., Tsurutani, B. T., & Vasyliunas, V. M. (1994). What is a geomagnetic storm? *Journal of Geophysical Research*, *99*(A4), 5771–5792. https://doi.org/10.1029/93JA02867

Gonzalez, W. D., Tsurutani, B. T., Lepping, R. P., & Schwenn, R. (2002). Interplanetary phenomena associated with very intense geomagnetic storms. *Journal of Atmospheric and Solar-Terrestrial Physics*, *64*(2), 173–181. https://doi.org/10.1016/S1364-6826(01)00082-7

Gosling, J. T. (1990). Coronal mass ejections and magnetic flux ropes in interplanetary space. *Physics of Magnetic Flux Ropes*, *58*, 343–364. https://doi.org/10.1029/GM058p0343

Kilpua, E., Koskinen, H. E. J., & Pulkkinen, T. I. (2017). Coronal mass ejections and their sheath regions in interplanetary space. *Living Reviews in Solar Physics*, *14*(1), 5. https://doi.org/10.1007/s41116-017-0009-6

Kim, K.-H., Kim, G.-J., & Kwon, H.-J. (2018). Distribution of equatorial Alfvén velocity in the magnetosphere: A statistical analysis of THEMIS observations. *Earth, Planets and Space*, *70*(1), 1–7.

King, J. H., & Papitashvili, N. E. (2005). Solar wind spatial scales in and comparisons of hourly Wind and ACE plasma and magnetic field data. *Journal of Geophysical Research*, *110*, A02104. https://doi.org/10.1029/2004JA010649

Kletzing, C. A., Kurth, W. S., Acuna, M., MacDowall, R. J., Torbert, R. B., Averkamp, T., et al. (2013). The Electric and Magnetic Field Instrument Suite and Integrated Science (EMFISIS) on RBSP. *Space Science Reviews*, *179*(1–4), 127–181. https://doi.org/10.1007/s11214-013-9993-6

Mauk, B. H., Fox, N. J., Kanekal, S. G., Kessel, R. L., Sibeck, D. G., & Ukhorskiy, A. A. (2012). Science objectives and rationale for the Radiation Belt storm probes mission. In *The Van Allen Probes mission* (pp. 3–27). Boston, MA: Springer. https://doi.org/10.1007/978-1-4899-7433-4_2

Meng, X., Tsurutani, B. T., & Mannucci, A. J. (2019). The solar and interplanetary causes of superstorms (minimum *Dst* −250 nT) during the space age. *Journal of Geophysical Research: Space Physics*, *124*, 3926–3948. https://doi.org/10.1029/2018JA026425

Milan, S. E., Provan, G., & Hubert, B. (2007). Magnetic flux transport in the Dungey cycle: A survey of dayside and nightside reconnection rates. *Journal of Geophysical Research*, *112*, A01209. https://doi.org/10.1029/2006JA011642

Milan, S. E., Wild, J. A., Hubert, B., Carr, C. M., Lucek, E. A., Bosqued, J. M., & Slavin, J. A. (2006). Flux closure during a substorm observed by Cluster, Double Star, IMAGE FUV, SuperDARN, and Greenland magnetometers. *Annales Geophysicae*, *24*, 751–767. https://doi.org/10.5194/angeo-24-751-2006

Milan, S. E., Lester, M., Cowley, S. W. H., Oksavik, K., Brittnacher, M., Greenwald, R. A., et al. (2003). Variations in the polar cap area during two substorm cycles. *Annales Geophysicae*, *21*(5), 1121–1140. https://doi.org/10.5194/angeo-21-1121-2003

Øieroset, M., Phan, T. D., Drake, J. F., Eastwood, J. P., Fuselier, S. A., Strangeway, R. J., et al. (2019). Reconnection with magnetic flux pileup at the interface of converging jets at the magnetopause. *Geophysical Research Letters*, *46*, 1937–1946. https://doi.org/10.1029/2018GL080994

Pollock, C. J., Burch, J. L., Chasapis, A., Giles, B. L., Mackler, D. A., Matthaeus, W. H., & Russell, C. T. (2018). Magnetospheric multiscale observations of turbulent magnetic and electron velocity fluctuations in Earth's magnetosheath downstream of a quasi-parallel bow shock. *Journal of Atmospheric and Solar-Terrestrial Physics*, *177*, 84–91. https://doi.org/10.1016/j.jastp.2017.12.006

Rijnbeek, R. P., Cowley, S. W. H., Southwood, D. J., & Russell, C. T. (1984). A survey of dayside flux transfer events observed by ISEE 1 and 2 magnetometers. *Journal of Geophysical Research*, *89*(A2), 786–800. https://doi.org/10.1029/JA089iA02p00786

Russell, C. T., Anderson, B. J., Baumjohann, W., Bromund, K. R., Dearborn, D., Fischer, D., et al. (2016). The magnetospheric multiscale magnetometers. *Space Science Reviews*, *199*, 189–256. https://doi.org/10.1007/s11214-014-0057-3

Russell, C. T., & Elphic, R. C. (1979). ISEE observations of flux transfer events at the dayside magnetopause. *Geophysical Research Letters*, *6*(1), 33–36. https://doi.org/10.1029/GL006i001p00033

Russell, C. T. (1972). The configuration of the magnetosphere. In E. R. Dyer (Ed.), *Critical problems of magnetospheric physics* (pp. 1–16). Washington, DC: National Academy of Sciences.

Russell, C. T., & Qi, Y. (2020). Flux ropes are born in pairs: An outcome of interlinked, reconnecting flux tubes. *Geophysical Research Letters*, *47*(15), e2020GL087620. https://doi.org/10.1029/2020GL087620

Sarantos, M., & Slavin, J. A. (2009). On the possible formation of Alfvén wings at Mercury during encounters with coronal mass ejections. *Geophysical Research Letters*, *36*, L04107. https://doi.org/10.1029/2008GL036747

Shue, J.-H., Chao, J. K., Fu, H. C., Russell, C. T., Song, P., Khurana, K. K., & Singer, H. J. (1997). A new functional form to study the solar wind control of the magnetopause size and shape. *Journal of Geophysical Research*, *102*(A5), 9497–9511. https://doi.org/10.1029/97JA00196

Shue, J.-H., Song, P., Russell, C. T., Steinberg, J. T., Chao, J. K., Zastenker, G., et al. (1998). Magnetopause location under extreme solar wind conditions. *Journal of Geophysical Research*, *103*(A8), 17,691–17,700. https://doi.org/10.1029/98JA01103

Singer, H., Matheson, L., Grubb, R., Newman, A., & Bouwer, D. (1996). *Monitoring space weather with the GOES magnetometers* (Vol. 2812, pp. 299–308). Paper presented at Proceedings of the SPIE 2812, GOES-8 and Beyond. https://doi.org/10.1117/12.254077

Slavin, J. A., Middleton, H. R., Raines, J. M., Jia, X., Zhong, J., Sun, W.-J., et al. (2019). MESSENGER observations of disappearing dayside magnetosphere events at Mercury. *Journal of Geophysical Research: Space Physics*, *124*, 6613–6635. https://doi.org/10.1029/2019JA026892

Slavin, J. A., & Holzer, R. E. (1981). Solar wind flow about the terrestrial planets 1. Modeling bow shock position and shape. *Journal of Geophysical Research*, *86*(A13), 11,401–11,418. https://doi.org/10.1029/JA086iA13p11401

Slavin, J. A., Imber, S. M., Boardsen, S. A., Di Braccio, G. A., Sundberg, T., Sarantos, M., et al. (2012). MESSENGER observations of a flux-transfer-event shower at Mercury. *Journal of Geophysical Research*, *117*, A00M06. https://doi.org/10.1029/2012JA017926

Sonnerup, B. U. O., & Scheible, M. (1998). Minimum and maximum variance analysis. In G. Paschmann & P. W. Daly (Eds.), *Analysis methods for multi-spacecraft data, ISSI Scientific Report SR-001* (pp. 185–220). Bern, Switzerland: International Space Science Institute.

Stephens, G. K., Sitnov, M. I., Ukhorskiy, A. Y., Roelof, E. C., Tsyganenko, N. A., & Le, G. (2016). Empirical modeling of the storm time innermost magnetosphere using Van Allen Probes and THEMIS data: Eastward and banana currents. *Journal of Geophysical Research: Space Physics*, *121*, 157–170. https://doi.org/10.1002/2015JA021700

Torbert, R. B., Burch, J. L., Phan, T. D., Hesse, M., Argall, M. R., Shuster, J., et al. (2018). Electron-scale dynamics of the diffusion region during symmetric magnetic reconnection in space. *Science*, *362*(6421), 1391–1395. https://doi.org/10.1126/science.aat2998

Tsyganenko, N. A., & Sitnov, M. I. (2007). Magnetospheric configurations from a high-resolution data-based magnetic field model. *Journal of Geophysical Research*, *112*, A06225. https://doi.org/10.1029/2007JA012260

Turner, D. L., Kilpua, E. K. J. J., Hietala, H., Claudepierre, S. G., O'Brien, T. P., Fennell, J. F., et al. (2019). The response of Earth's electron radiation belts to geomagnetic storms: Statistics from the Van Allen Probes era including effects from different storm drivers. *Journal of Geophysical Research: Space Physics*, *124*, 1013–1034. https://doi.org/10.1029/2018JA026066

Turner, D. L., Shprits, Y., Hartinger, M., & Angelopoulos, V. (2012). Explaining sudden losses of outer radiation belt electrons during geomagnetic storms. *Nature Physics*, *8*(3), 208–212. https://doi.org/10.1038/nphys2185

Ukhorskiy, A. Y., Anderson, B. J., Brandt, P. C., & Tsyganenko, N. A. (2006). Storm time evolution of the outer radiation belt: Transport and losses. *Journal of Geophysical Research*, *111*, A11S03. https://doi.org/10.1029/2006JA011690

Wang, Y. L., Elphic, R. C., Lavraud, B., Taylor, M., Birn, J., Russell, C. T., et al. (2006). Dependence of flux transfer events on solar wind conditions from 3 years of Cluster observations. *Journal of Geophysical Research*, *111*, A04224. https://doi.org/10.1029/2005JA011342

Wanliss, J. A., & Showalter, K. M. (2006). High-resolution global storm index: Dst versus SYM-H. *Journal of Geophysical Research*, *111*, A02202. https://doi.org/10.1029/2005JA011034

Winslow, R. M., Anderson, B. J., Johnson, C. L., Slavin, J. A., Korth, H., Purucker, M. E., et al. (2013). Mercury's magnetopause and bow shock from MESSENGER Magnetometer observations. *Journal of Geophysical Research: Space Physics*, *118*, 2213–2227. https://doi.org/10.1002/jgra.50237

Winter, L. M. (2019). Geomagnetically induced currents from extreme space weather events. *Geomagnetically induced currents from the Sun to the power grid*, 195–203.

Xiao, C. J., Pu, Z. Y., Ma, Z. W., Fu, S. Y., Huang, Z. Y., & Zong, Q. G. (2004). Inferring of flux rope orientation with the minimum variance analysis technique. *Journal of Geophysical Research*, *109*, A11218. https://doi.org/10.1029/2004JA010594